ACS Photonics

Article

Cite This: ACS Photonics 2020, 7, 288−295

pubs.acs.org/journal/apchd5

Efficient Optical Quantification of Heterogeneous Emitter Ensembles

S. Alex Breitweiser,[†,‡] Annemarie L. Exarhos,[†,§] Raj N. Patel,[†] Jennifer Saouaf,[†] Benjamin Porat,[†] David A. Hopper,[†,‡] and Lee C. Bassett*[,†]

[†]Quantum Engineering Laboratory, Department of Electrical and Systems Engineering, University of Pennsylvania, 200 South 33rd Street, Philadelphia, Pennsylvania 19104, United States

[‡]Department of Physics and Astronomy, University of Pennsylvania, 209 South 33rd Street, Philadelphia, Pennsylvania 19104, United States

Supporting Information

ABSTRACT: Defect-based quantum emitters in solid-state materials offer a promising platform for quantum communication and sensing. Confocal fluorescence microscopy techniques have revealed quantum emitters in a multitude of host materials. The ability to quickly and accurately survey emitter ensembles is important for characterizing these new quantum emitter systems. In some materials, however, optical properties vary widely among emitters, even within the same sample. In these cases, traditional ensemble fluorescence measurements are confounded by heterogeneity, whereas individual defect-by-defect studies are impractical. Here we describe a method to quantitatively and systematically analyze the properties of heterogeneous emitter ensembles using large-area photoluminescence maps. We apply this method to study the effects of sample treatments on emitters in hexagonal boron nitride, and we find that low-energy (3 keV) electron irradiation creates emitters, whereas high-temperature (850 °C) annealing in an inert gas environment brightens emitters.

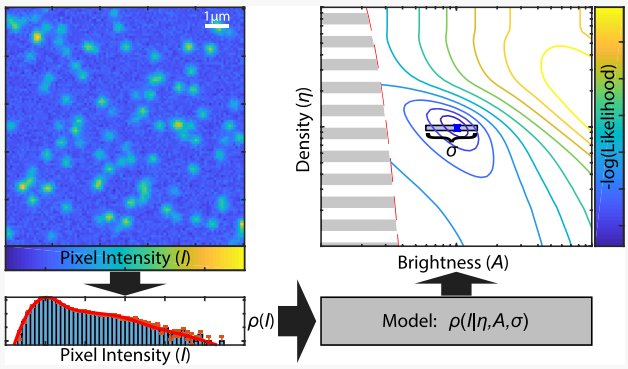

KEYWORDS: *quantum emitters, optical characterization, emitter ensembles, hexagonal boron nitride, fluorescence microscopy, statistical image analysis*

As optically addressable spin qubits, defects in solid-state materials have been used to facilitate the storage and transmission of quantum information and precisely sense temperature, strain, and electromagnetic fields at the nanoscale.[1,2] The most prominent of these defects, such as the nitrogen-vacancy (NV) center in diamond, act as point-source quantum emitters and have a well-understood chemical structure that can be controllably formed in high-purity host materials. Historically, the availability of homogeneous emitter ensembles has been essential for their identification[3,4] and development for quantum applications.[5,6] By the use of confocal microscopy, however, it is possible to screen many potential host materials for individual quantum emitters. Indeed, quantum emitters have been found in an ever-increasing number of materials, including silicon carbide, zinc oxide, gallium nitride, hexagonal boron nitride (hBN), and transition-metal dichalcogenides.[7,8] In these emerging materials platforms, ensemble studies have proven to be more difficult. Studies are confounded by difficulty synthesizing the host material and controlling its purity, uncertainty about the background impurity levels, unknown chemical structure of the emitters, and often substantial heterogeneity of the emitters themselves. Furthermore, traditional ensemble studies, in which average photoluminescence (proportional to density multiplied by brightness) is used to make quantitative comparisons, are not sufficient for such heterogeneous emitters. New techniques are required that can distinguish brightness from density while still being efficient enough to study large ensembles across wide field images.

Hexagonal boron nitride, a two-dimensional (2D) semiconductor with an indirect band gap of 5.955 eV[9] and a rich taxonomy of defects,[10,11] is a prototypical example. It is already a ubiquitous dielectric in van der Waals heterostructures[12] and is emerging as a versatile platform for nanophotonics.[13] Recent experiments have identified pointlike quantum emission at visible to near-infrared wavelengths from hBN.[14−19] These emitters appear to be robust to the preparation method, having been found in hBN samples of dispersed nanoflakes, exfoliated bulk crystals, and thin films grown by chemical vapor deposition in thicknesses ranging from monolayer to bulk.[20] The emitters can be spectrally tuned by strain[21] and electric fields,[22] and they can be coupled to photonic nanocavities and

Received: December 3, 2019
Published: December 17, 2019

Downloaded via UNIV OF PENNSYLVANIA on December 31, 2020 at 18:34:43 (UTC).
See https://pubs.acs.org/sharingguidelines for options on how to legitimately share published articles.

© 2019 American Chemical Society

DOI: 10.1021/acsphotonics.9b01707
ACS Photonics 2020, 7, 288−295

dielectric antennas that direct and enhance the emission.[23,24] Some emitters in hBN also exhibit magnetically sensitive fluorescence at room temperature, indicating the potential for coherent spin control.[25]

However, the underlying electronic and chemical structures of emitters in hBN have remained elusive, partly because of their heterogeneous properties. The brightness, density, polarization, and spectral distribution of emitters vary widely, both among and within samples.[15,16,18] Electronic structure calculations have considered multiple defect candidates as possible sources of the emission,[11,26−28] but none can fully account for the observations. A plethora of treatments—including annealing,[14] plasma[29,30] and chemical[17] etching, irradiation by electrons (both low- and high-energy)[15,31,32] and ions,[17] strain engineering,[33] and ion-beam milling[34]—have been used to create and stabilize emitters. Analyzing the effects of these experiments has to date relied on individually cataloguing large numbers of heterogeneous emitters by hand. However, these studies are prone to sampling bias and have not been able to capture enough emitters to make statistically rigorous quantitative comparisons. In this work, we developed a versatile and efficient framework for quantifying the optical properties of heterogeneous emitter ensembles from large-area photoluminescence (PL) maps and applied it to analyze two common sample treatments in hBN: high-temperature annealing under an inert gas environment and low-energy electron beam irradiation. We found that low-energy irradiation was sufficient to create new emitters, while annealing primarily brightened existing ensembles without significantly changing their density.

1. MODEL AND ANALYSIS

As an example of the type of data we wish to analyze, Figure 1 shows optical and electron microscope images of an hBN flake as well as PL maps from a suspended region taken before treatment, after electron irradiation, and after subsequent annealing. The pretreatment map reveals multiple emitters of similar brightness. After electron beam irradiation, many more emitters are visible, with some now much brighter than others. After annealing, the apparent number of emitters further increases, with the brightest emitters again much brighter than the dimmest. While it is generally difficult to track individual emitters across treatments, the Supporting Information includes a data set where certain emitter clusters persisted before and after irradiation and some isolated emitters appeared in the same location with similar dipole orientations before and after annealing.

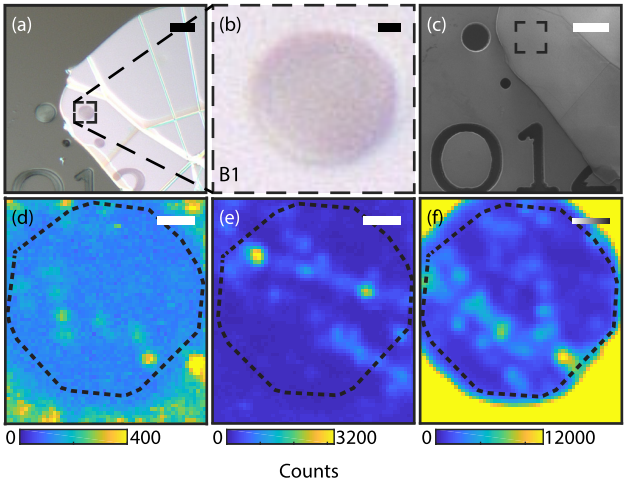

Figure 1. (a, b) Optical and (c) electron microscope images of a flake of hBN on a patterned Si/SiO_2 substrate. The magnified image in (b) is outlined with a dashed line in (a) and shows a suspended region of hBN, labeled as Region B1 later in the text. The same region is outlined again in the electron microscope image in (c). Profilometer measurements, available in the Supporting Information, confirmed that the flake was flat near this region. (d−f) PL maps of the same region (d) before treatment, (e) after electron irradiation, and (f) after high-temperature argon annealing. The suspended region used in subsequent analysis is outlined with a dashed line in (d−f). Scale bars represent (a, c) 10 μm and (b, d−f) 1 μm.

Rather than attempting to identify and track every emitter in these scans, we fit the data using a model that predicts the statistical properties of heterogeneous point-source emitter ensembles. The procedure distills the map into a distribution of pixel intensities, which is fitted to produce an estimate of the density and brightness distribution of emitters present in the region. The model assumes that emitters appear as diffraction-limited point sources with uniform spatial distribution and with brightnesses drawn from a weighted mixture of normal distributions. In the following analysis and discussion, we interpret these normal distributions as multiple emitter "families", each characterized by a spatial density, mean brightness, and brightness variance. We stress, however, that this is purely a phenomenological description of the observed emitter distributions; it does not necessarily reflect a classification of the underlying chemical or electronic structure of these emitters.

The model produces a probability density for the intensity of pixels in the region,

$$p(I|\eta_m, A_m, \sigma_m, \lambda) = \overset{M}{\underset{m=1}{*}}\left(\sum_n P_n(\eta_m) p_n(I|A_m, \sigma_m)\right) * \mathrm{Poiss}(I|\lambda) \quad (1)$$

where $m \in [1, M]$ labels each emitter family with corresponding density η_m, average brightness A_m, and brightness standard deviation σ_m; λ parametrizes the brightness of the Poissonian background; $P_n(\eta_m)$ is the probability of having n emitters of family m within the region of interest; $p_n(I \mid A_m, \sigma_m)$ is the probability density for pixels as a function of brightness I resulting from n emitters from family m; Poiss($I \mid \lambda$) is the probability density resulting from a Poissonian background with average intensity λ; and $*_{m=1}^{M}$ and $*$ represent convolutions. The Supporting Information provides a derivation of this model along with explicit expressions for P_n and p_n. In general, the form of these functions depends on assumptions regarding the emitters' spatial and brightness distributions. We assume a uniform spatial distribution and a normal brightness distribution for each emitter family, but the model can be adapted to any spatial or brightness distribution. The model is probabilistic and ignores spatial information to take advantage of the statistical power of large maps; therefore, it reveals information about ensemble properties of the collection of emitters present in a sample rather than information about individual emitters.

We fit this model to the observed pixel brightness distributions using Differential Evolution[35] to optimize the χ^2 statistic. The number of families, M, is chosen to minimize the Akaike information criterion (AIC), which measures fit quality

DOI: 10.1021/acsphotonics.9b01707
ACS Photonics 2020, 7, 288−295

while penalizing overfitting from a high number of families. More details are presented in the Supporting Information.

To test this procedure, we compared the fit results from the model against the parameters of known emitter distributions. Figure 2a shows a PL map of NV centers in bulk single-crystal

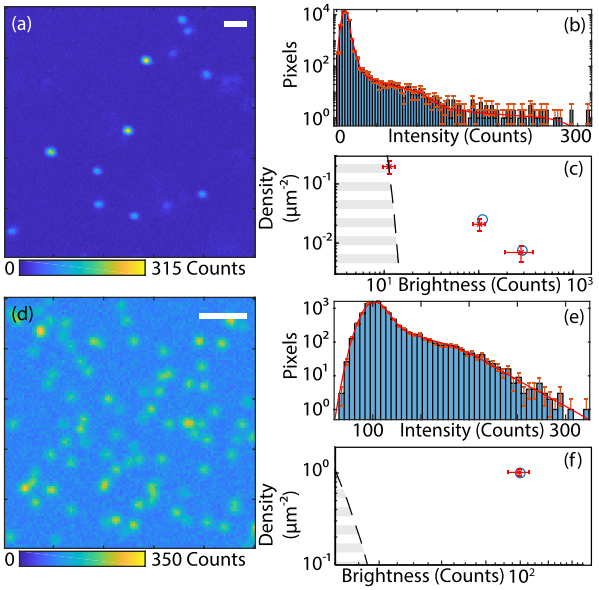

Figure 2. Testing the quantitative model. (a) PL map of NV centers in single-crystal bulk diamond. Several NV centers, both aligned and misaligned to the excitation laser polarization, are in focus. (b) Histogram of pixel intensities (points) from (a) together with the best fit of the quantitative model (red curve). (c) Emitter family parameters (red crosses) corresponding to the best-fit curve in (b). The best-fit background is represented by a dashed curve bounding a hatched region where the model cannot resolve emitter families from noise. Known values for the density and brightness corresponding to NV centers with different dipole orientations are shown as blue circles. (d) Simulated PL map for a single family of emitters based on parameters similar to hBN maps. (e, f) Corresponding pixel intensity histogram, fit, and emitter family parameter plot as in (b) and (c). The underlying simulation values for the emitter family are indicated by the blue circle. Scale bars in (a) and (d) represent 2 μm. Error bars in (c) and (f) represent 95% confidence intervals.

diamond, with a focus plane located approximately 3 μm from the planar (100)-oriented surface. The laser polarization is aligned to the dominant optical excitation dipole for the NV center at the center of the map. There are three aligned and 10 misaligned NV centers in this 400 μm^2 region, with reproducible peak intensities of ~300 counts (30 kCts/s) and ~120 counts (12 kCts/s), respectively. These peak intensities include a background of ~10 counts (1 kCts/s), which appears to be uniform across the map. In addition, some non-pointlike emission appears in Figure 2a, which may result from out-of-focus NV centers or surface contamination.

Figure 2b shows the histogram of pixel intensities from this map as well as the result of fitting the model to this distribution. The fitting procedure identifies three emitter families, whose density and brightness parameters are shown in Figure 2c. Two of these families are within one standard uncertainty of both the density and brightness of the aligned and misaligned NV centers identified in the map after the background is taken into account. In addition, the best-fit background of 10.064(92) counts is close to the ~10 counts measured by eye from the PL map and is represented in Figure 2c by a dashed curve in brightness/density space. For values of brightness and density below this curve, the model cannot reliably distinguish emitter families from noise. One additional emitter family appears close to the noise floor in Figure 2c; this may arise from weak non-point-source PL features in the map.

The low density and reproducible brightness of NV centers in diamond make maps like Figure 2a easy to interpret by eye. A simulated data set with less ideal conditions, similar to the hBN PL maps in Figure 1d–f, is shown in Figure 2d. Here the density of emitters is much greater, such that some emitters overlap and are indistinguishable by eye, and the brightness of emitters has a wide distribution. In addition, the background intensity is comparable to the brightness of emitters. Nevertheless, the fitting procedure captures the pixel intensity distribution well, and the analysis yields a single emitter family with parameters that agree with the underlying simulation parameters, as shown in Figure 2e,f. Similar analyses for simulations of multiple emitter families are presented in the Supporting Information.

2. RESULTS

A list of hBN regions studied in this work and the treatments applied to them is presented in Table 1 (see Methods for details of sample preparation, treatments, and data acquisition). PL maps from each region for each stage of treatment were analyzed using our model; regions were imaged under identical conditions in each stage. The fitting results from four representative regions are presented in Figure 3 and discussed below. Raw PL map data and analysis of additional regions are available in the Supporting Information.

Table 1. Summary of hBN Regions and Treatment Sequences

region	thickness	first treatment	second treatment
A1	215 nm	low-dose e^- irr.	Ar anneal
A2	240 nm	low-dose e^- irr.	Ar anneal
B1	390 nm	high-dose e^- irr.	Ar anneal
B2	250–350 nm	high-dose e^- irr.	Ar anneal
C1	630 nm	indirect e^- irr.	Ar anneal
D1	n.a.[a]	Ar anneal	low-dose e^- irr.[b]

[a]Thickness information is not available for this region. [b]The radiation dose in this region was 4×10^{15} e^-/cm^2.

We first consider the effect of electron irradiation in a scanning electron microscope (SEM). Region C1 received no direct exposure to the electron beam, although it was present in the instrument chamber to measure effects of the ambient chamber conditions. As shown in Figure 3a, this region saw a small decrease in the density of pre-existing emitters, although it was within the uncertainty of the fits. Some decrease due to photobleaching from successive PL scans is expected. In addition, the appearance of a single bright emitter resulted in the detection of a new family with high brightness and low density; we tentatively attribute this isolated event to stray ions accelerated in the column. Regions A1 and B1 received low and high doses of direct electron irradiation, respectively. Region A1 saw a small increase in the density of its pre-existing emitter family, although the increase was within the fit uncertainty (see Figure 3b). The high-dose region B1 considered in Figure 3c is the same one presented in Figure 1; it showed a significant increase in the density of its pre-

DOI: 10.1021/acsphotonics.9b01707
ACS Photonics 2020, 7, 288–295

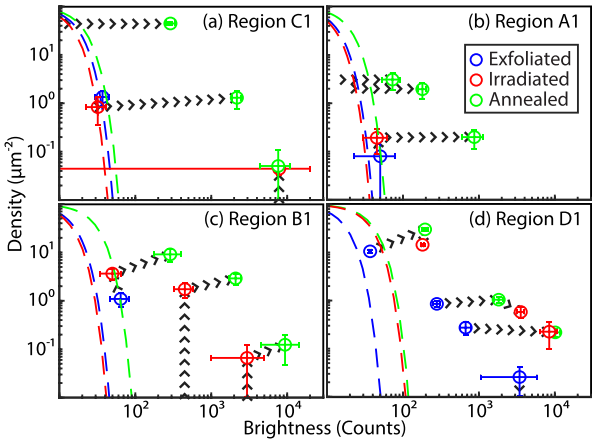

Figure 3. Best-fit parameters after each treatment stage for four representative hBN regions from Table 1. The estimated density and brightness of each emitter family are represented as a circle in blue (pretreatment), red (postirradiation), or green (postannealing) based on which stage of the treatment process the flake is in. Region D1 in (d) was annealed prior to irradiation, whereas all of the other regions were irradiated first. Arrows indicate potential evolution of these emitter families from the treatment process based on qualitative observations. A noise floor, determined by the best-fit background for each map, is displayed as a dashed line and determines the lower limit for detecting emitter families. Error bars represent 95% confidence intervals in the best-fit parameter values.

existing emitter family along with the appearance of two new families of higher brightness.

Regions A1, B1, and C1 were all annealed after irradiation under the same conditions as described in Methods. The fit results for region B1 show that there are three emitter families both before and after annealing, with approximately the same densities but systematically higher brightnesses. The simplest interpretation of these results is that each family became brighter without a significant change in density. Analysis of regions A1 and C1 also uncovered postannealing families with densities similar to those of the pre-existing families but with higher brightnesses, consistent with this interpretation. However, these regions also contained new dim, dense emitter families after annealing. Considering the relative change in brightness for pre-existing emitter families, we propose that these emitters existed before annealing but were below the noise floor and only became bright enough to be captured by the model after annealing. No new families were detected after annealing for the high-dose Region B1. However, the dimmest family saw a density increase at the edge of statistical significance, and the background showed a large increase not seen in the low-dose or nonirradiated region. Both of these features could be indicative of a dim, dense family that cannot adequately be resolved in the data. In Figure 3, we indicate the possible evolution of emitter families under annealing via dashed lines.

Region D1 was first annealed, followed by a low dose of irradiation; its analysis is shown in Figure 3d. The pretreatment analysis detected four families of emitters already present in the region; we attribute the greater number of pretreatment emitter families here to alternate sample preparation, as this flake was exfoliated from a different bulk crystal and underwent postexfoliation O_2 plasma cleaning. Recent studies have shown that plasma treatments can create new emitters.[29,30] After annealing, the brightest family, which consisted of a single emitter, disappeared, which we attribute to photobleaching. The other three families can again be seen to increase in brightness. Similar to region B1, the dimmest emitter family also saw a slight increase in density, and the background saw a large increase. After irradiation, the emitter parameters did not exhibit a significant change. This is consistent with the results for Region A1, which also received a low irradiation dose; the expected increase in emitter density is small compared with the large densities already present in Region D1 after annealing.

In order to compare results from different regions and to generate a more rigorous statistical understanding of the treatment effects, we consider the full emitter brightness distribution extracted from the analysis of each region. The brightness distribution of emitters is obtained by summing the individual contributions of the different families weighted by their densities, $\sum_m \eta_m \mathcal{N}(I|A_m, \sigma_m^2)$, where $\mathcal{N}(I|A, \sigma^2)$ is a normal distribution on I with mean A and variance σ^2. Because of the wide range of brightnesses observed, the results are best shown on a logarithmic brightness scale. Thus, we present the results as a log-space probability density,

$$\Lambda(I) = I \sum_m \eta_m \mathcal{N}(I|A_m, \sigma_m^2) \tag{2}$$

where the additional factor of I accounts for the logarithmic spacing of brightnesses, correcting the visual weight of the plotted distribution.

Figure 4 shows this distribution for regions that received irradiation followed by annealing. In the pretreatment distributions of Figure 4a, we observe a localized peak at around 50 counts (~400 Cts/s), with very few emitters brighter than 1000 counts (~8 kCts/s). Any emitters with brightness below ~30 counts cannot be resolved from the background noise (indicated by dashed lines). Figure 4b shows the results for the same regions after irradiation. We observe a much larger peak at around 70 counts as well as new peaks appearing with higher brightness. Finally, the postannealing distributions shown in Figure 4c are much broader, with emitters found from the noise floor of ~30 counts to ~10^4 counts (~800 kCts/s).

To better visualize the treatment effects, Figure 4d,e presents the differences between the distributions before and after irradiation and annealing, respectively. We observe from Figure 4d that irradiation produced an almost uniform increase in the density of emitters and that regions B1 and B2, which received larger doses, saw larger density increases than regions A1 and A2. Annealing showed a qualitatively different effect, with densities decreasing at lower brightness and increasing at higher brightness in Figure 4e. There is a small overall increase in density; this, as well as the overall broadening of the distribution, can tentatively be attributed to the dim, dense emitters that might be below the noise floor in preannealing fits.

3. DISCUSSION

3.1. Irradiation. In agreement with qualitative observations of images such as those in Figure 1 and with the observations of earlier studies,[15,31,36] our quantitative analysis shows that low-energy electron irradiation increases the emitter density, creating emitters of low-to-intermediate brightness. However, the underlying mechanism for emitter creation due to electron-beam irradiation remains unknown. For comparison, typical methods to create NV centers in diamond use electrons of

DOI: 10.1021/acsphotonics.9b01707
ACS Photonics 2020, 7, 288−295

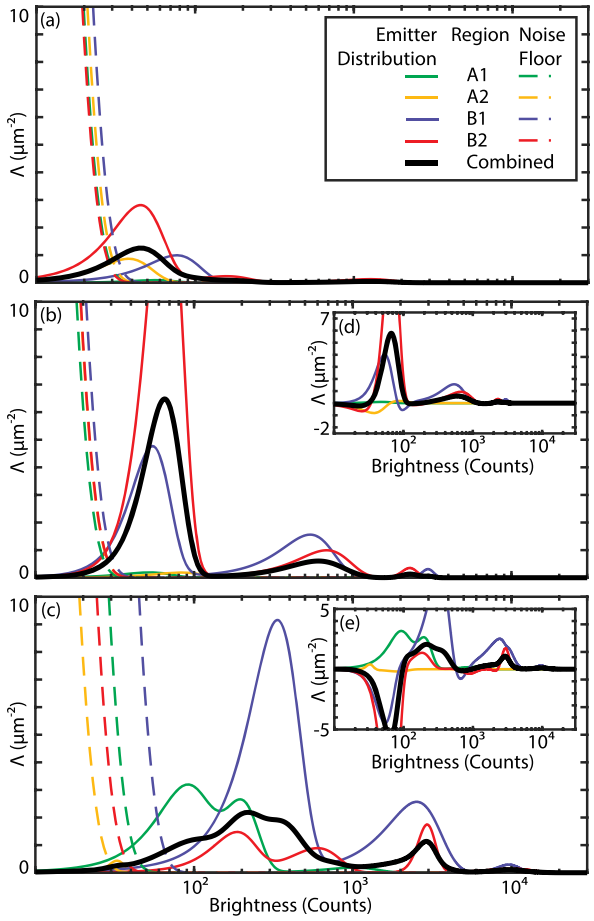

Figure 4. Emitter brightness distributions for regions that received direct irradiation prior to annealing; distributions for each region (a) before treatment, (b) after irradiation, and (c) after annealing are plotted as thin colored curves for each region as indicated in the legend, with the combined distribution for all regions shown as a thick black curve. Dashed curves indicate the background noise floor for each region. Inset panels (d) and (e) show the changes in the distributions from pretreatment to postirradiation and postirradiation to postannealing, respectively. It should be noted that since the brightness is shown on a logarithmic scale, the log-space probability density is shown (see the text for details).

sufficient energy to create vacancies in the lattice, with subsequent annealing treatments to combine them with nitrogen defects to create NV centers. In contrast, the electron energies used here were much lower than the minimum energy for creating monovacancies in hBN,[37] corresponding to an accelerating voltage of 80 kV. One possibility is that these new emitters were created by stray ions accelerated in the chamber, which would have sufficient energy to create vacancies. Using a similar irradiation procedure, however, Vogl et al. found that emitters are created uniformly throughout samples thinner than the stopping range of the electrons, which is on the order of a micrometer for the 3 keV energy of our electron beam.[36] Ions at this energy would travel only a few nanometers into the hBN, and they would appear independently of beam exposure. Combined with our observation that the number of emitters created increases with electron dose, this argues for a creation mechanism based on interactions between the electrons and hBN rather than accidental implantation of impurity ions in the SEM chamber. The electrons might have sufficient energy to perturb the placement of interstitial atoms or to cause reconstruction of edges or extended defects. This interpretation could support a recent proposal that dangling bonds on hBN edges are responsible for quantum emission in this material.[38] Alternatively, charge trapping may cause emitter activation, as suggested in previous studies.[33,39] Irradiation could reconfigure the charge state of existing defects, converting them into a fluorescent configuration, or the reconfiguration of nearby charge traps could alter the (non)radiative relaxation pathways relevant for the visible PL.

3.2. Annealing. Similarly, the role of annealing on hBN's quantum emission is poorly understood. For comparison, annealing is used in diamond to increase the mobility of lattice vacancies, which combine with substitutional nitrogen atoms to create NV centers. Whereas qualitative assessment of PL maps like those in Figure 1 gives the impression that annealing also creates emitters in hBN, our quantitative analysis indicates that the primary effect of annealing is to brighten existing ensembles without significantly changing the density of emitters. The brightness increase induced by annealing is around 1 order of magnitude regardless of the emitters' original brightness—a surprising result given that the emitter brightnesses span several orders of magnitude. Some regions also saw the appearance of dim, dense emitter families after annealing; even for regions where such families were not detected, a larger increase in the background intensity and in the density of pre-existing families point to the possibility of dim emitters that were subsumed into the background and excluded from our analysis. If it is assumed that these dim emitters were also brightened by annealing, it is possible they were present before annealing but not detected because they were below the noise floor.

The brightness enhancement could be explained by an increase in the emitters' quantum efficiency. Potentially, annealing could affect the concentration of nonemissive defects in the sample, which would modify the nonradiative decay pathways for the emissive defects. This interpretation is supported by the varied quantum efficiencies for hBN emitters reported in the literature, which range from 6%[24] to 87%.[40] This could also explain why the brightness increase is consistently around an order of magnitude regardless of the initial brightness of the emitters.

While a systematic increase in brightness due to annealing is the simplest interpretation of our observations, we cannot rule out all other potential effects. Studies using rapid thermal annealing rather than a tube furnace saw an increase in zero-phonon line intensity and noted that longer annealing times led to spatial diffusion of emitters.[30] Such diffusion, combined with the increased brightness of emitters, could give the impression of bright emitters being created simultaneously with dim emitters being destroyed. The mobility of point defects or impurities in the lattice during annealing might explain these effects, either by moving the underlying defects or otherwise modifying the emitters' chemical structure. Of the single-atom vacancies and interstitial defects, only boron vacancies are expected to become mobile around 800 °C, with nitrogen vacancies requiring temperatures in excess of 1500 °C and interstitial defects already being mobile near room temperature.[11] The framework presented here could be used to study the temperature dependence of annealing effects for comparison with theoretical calculations of the onset of defect mobility for different species.

DOI: 10.1021/acsphotonics.9b01707
ACS Photonics 2020, 7, 288−295

4. CONCLUSION

We have presented a method to efficiently assess the optical properties of statistically large heterogeneous quantum-emitter ensembles. Tracking systematic variations between samples or between treatments offers quantitative insight into the mechanisms at play. In the case of hBN, electron irradiation provides an accessible and controllable method for creating emitters in otherwise dark samples. For samples with dim emitters, annealing may provide a way to brighten emitters.

While this study focused on the brightness and density of emitters, the model can also be expanded to capture other properties of quantum emitters, such as their dipole orientation and spectral distribution. Previous work studied the alignment of emitter dipole orientations to the crystallographic axes of hBN.[16] By extending our model to include polarized emitter families and comparing to polarization-resolved data, we could leverage the statistical power of much larger emitter ensembles to study the distribution of dipole orientations. A similar extension of our model could account for the emitters' spectra; including spectrally resolved data could reveal phenomena such as zero-phonon line clustering, which has been observed in multiple recent studies.[41−43] By adaptation of the underlying spatial probability distribution functions, the model can be further extended to account for emitters clustering near edges or other extended defects.

This methodology can be applied to any material hosting point-source emitters, including dispersed nanoparticles and fluorescent molecules. It is is particularly relevant for 2D materials, where heterogeneity is prevalent and advances in fluorescence imaging have enabled the efficient acquisition of emission maps from large sample regions. Such wide-field techniques have been used to study the role of the annealing temperature in NV center quenching and formation[44] as well as to study the spectral and temporal properties of emitters in hBN.[42,43] However, these studies relied on algorithms designed to identify and track individual emitters, which cannot handle significant heterogeneity among emitters and are expected to fail at high emitter densities and low emitter brightnesses. Combining these wide-field imaging techniques with the approach presented here would facilitate efficient and accurate screening of large ensembles of heterogeneous emitters, an important step for the identification and study of new platforms for defect-based quantum technologies.

5. METHODS

Flakes of hBN were exfoliated from bulk single crystals (HQ Graphene) onto patterned Si wafers with a 90 nm layer of thermal SiO_2 on top. The flakes hosting regions A1−A2, B1−B2, C1−C3, and E1 were first exfoliated onto a polydimethylsiloxane stamp and then transferred onto the silicon substrate at a temperature of 50 °C. The flakes hosting regions D1−D3 were prepared following the method used in refs 16 and 25 and further underwent O_2 plasma cleaning in an oxygen barrel asher (Anatech SCE 108). Flake thicknesses were measured using a stylus profilometer and ranged from <100 to >600 nm, with most of the flakes falling between 200 and 400 nm. Of particular interest are regions suspended over holes etched into the substrate (>6 μm deep), where emitters show a greater contrast with the background and better isolation from substrate-dependent effects.

Suspended regions were identified using an optical microscope and alternately exposed to a 3 keV electron beam (FEI Strata DB235 FIB SEM) and annealed in a tube furnace under flowing argon gas. The electron beam was rastered over a known area, with the dosage calculated from the area size and the approximate beam current. Low-dose irradiated regions, with the exception of D1, received fluences on the order of 2×10^{16} e^-/cm^2, while high-dose regions received approximately 2×10^{17} e^-/cm^2. Region D1 received a dose of 4×10^{15} e^-/cm^2. Calculated fluences for all of the regions are available in the Supporting Information. The annealing ramp rate was set to 10 °C min^{-1}, leading to a heating period of ∼1.5 h to reach 850 °C. Once 850 °C was reached, the temperature was maintained for 30 min, after which the sample was allowed to cool to room temperature over the course of several hours. Argon gas was flowed from before heating until after cooling of the sample to ensure complete evacuation of other gases from the chamber while the sample temperature was elevated.

Samples were mounted in a custom-built confocal fluorescence microscope, where PL was stimulated with a 592 nm continuous-wave laser (MPB Communications, VFL-592) and collected between 650 and 900 nm. For this study, the preobjective power was fixed to ∼500 μW, and the laser polarization was rotated using a half-wave plate (Newport 10RP12-16) and corrected for birefringence. PL maps were recorded for each region with multiple laser polarizations, registered, and added together to create a polarization-independent PL map. Maps were acquired for each region at each stage of the treatment process and compared to a point-emitter model, as described in the main text, to determine the underlying microscopic parameters.

For the NV-center reference scan in Figure 2a, an electronic-grade type-IIa synthetic diamond from Element Six was irradiated with 2 MeV electrons at a fluence of 10^{14} e^-/cm^2 and then annealed in forming gas at 800 °C for 1 h. The diamond sample was mounted in another custom-built confocal fluorescence microscope. A 532 nm continuous-wave laser (Laser Quantum, Gem 532) was used to optically excite the NV centers, and the fluorescence was collected with a 650 nm long-pass filter. The polarization was similarly varied using a half-wave plate, and the preobjective laser power was set to 500 μW.

A layer of NV centers was found approximately 3 μm from the diamond surface, and the confocal depth was set to focus on the NV center at the center of the scan in Figure 2a. The laser polarization was set to maximize the PL from the central NV center. Because of the geometry of NV centers beneath a (100) diamond surface, all of the other NV centers in the sample were either aligned or misaligned with the excitation axis by the same angle.

■ ASSOCIATED CONTENT

Supporting Information

The Supporting Information is available free of charge at https://pubs.acs.org/doi/10.1021/acsphotonics.9b01707.

Profilometer measurement near region B1; PL maps of region B2 with persistent emitters identified; details of the emitter model used for fitting; additional simulation results; table of regions with additional information; additional emitter distributions obtained; full photoluminescence data sets with fit results (PDF)

DOI: 10.1021/acsphotonics.9b01707
ACS Photonics 2020, 7, 288−295

AUTHOR INFORMATION

Corresponding Author

*E-mail: lbassett@seas.upenn.edu.

ORCID

S. Alex Breitweiser: 0000-0002-0325-4765
David A. Hopper: 0000-0003-1965-690X
Lee C. Bassett: 0000-0001-8729-1530

Present Address

§A.L.E.: Department of Physics, Lafayette College, Easton, PA 18042, USA.

Notes

The authors declare no competing financial interest.

ACKNOWLEDGMENTS

The authors thank R. Grote for assistance with electron-beam irradiation. This work was supported by the National Science Foundation under award DMR-1922278 (SAB, RNP, and LCB) and the Army Research Office under award W911NF-15-1-0589 (ALE, RNP, JS, DAH, and LCB). BP acknowledges support from the Penn Undergraduate Research Mentoring program. We gratefully acknowledge use of facilities and instrumentation at the Singh Center for Nanotechnology supported by the National Science Foundation through the National Nanotechnology Coordinated Infrastructure Program (NNCI-1542153) and Penn's Materials Research Science and Engineering Center (DMR-1720530).

REFERENCES

(1) Awschalom, D. D.; Hanson, R.; Wrachtrup, J.; Zhou, B. B. Quantum technologies with optically interfaced solid-state spins. *Nat. Photonics* **2018**, *12*, 516.

(2) Atatüre, M.; Englund, D.; Vamivakas, N.; Lee, S.-Y.; Wrachtrup, J. Material platforms for spin-based photonic quantum technologies. *Nat. Rev. Mater.* **2018**, *3*, 38.

(3) Davies, G.; Hamer, M. F. Optical studies of the 1.945 eV vibronic band in diamond. *Proc. R. Soc. London, Ser. A* **1976**, *348*, 285.

(4) Loubser, J. H. N.; Van Wyk, J. A. Optical spin-polarisation in a triplet state in irradiated and annealed type 1B diamonds. *Diamond Res.* **1977**, *9*, 11−14.

(5) Acosta, V. M.; Bauch, E.; Ledbetter, M. P.; Santori, C.; Fu, K.-M.; Barclay, P. E.; Beausoleil, R. G.; Linget, H.; Roch, J. F.; Treussart, F.; et al. Diamonds with a high density of nitrogen-vacancy centers for magnetometry applications. *Phys. Rev. B: Condens. Matter Mater. Phys.* **2009**, *80*, 115202.

(6) Waldermann, F.; Olivero, P.; Nunn, J.; Surmacz, K.; Wang, Z.; Jaksch, D.; Taylor, R.; Walmsley, I.; Draganski, M.; Reichart, P.; et al. Creating diamond color centers for quantum optical applications. *Diamond Relat. Mater.* **2007**, *16*, 1887−1895.

(7) Aharonovich, I.; Englund, D.; Toth, M. Solid-state single-photon emitters. *Nat. Photonics* **2016**, *10*, 631.

(8) Bassett, L. C.; Alkauskas, A.; Exarhos, A. L.; Fu, K.-M. C. Quantum Defects by Design. *Nanophotonics* **2019**, *8*, 1867−1888.

(9) Cassabois, G.; Valvin, P.; Gil, B. Hexagonal boron nitride is an indirect bandgap semiconductor. *Nat. Photonics* **2016**, *10*, 262.

(10) McDougall, N. L.; Partridge, J. G.; Nicholls, R. J.; Russo, S. P.; McCulloch, D. G. Influence of point defects on the near edge structure of hexagonal boron nitride. *Phys. Rev. B: Condens. Matter Mater. Phys.* **2017**, *96*, 144106.

(11) Weston, L.; Wickramaratne, D.; Mackoit, M.; Alkauskas, A.; Van de Walle, C. Native point defects and impurities in hexagonal boron nitride. *Phys. Rev. B: Condens. Matter Mater. Phys.* **2018**, *97*, 214104.

(12) Geim, A. K.; Grigorieva, I. V. Van der Waals heterostructures. *Nature* **2013**, *499*, 419.

(13) Caldwell, J. D.; Aharonovich, I.; Cassabois, G.; Edgar, J. H.; Gil, B.; Basov, D. N. Photonics with hexagonal boron nitride. *Nat. Rev. Mater.* **2019**, *4*, 552.

(14) Tran, T. T.; Bray, K.; Ford, M. J.; Toth, M.; Aharonovich, I. Quantum emission from hexagonal boron nitride monolayers. *Nat. Nanotechnol.* **2016**, *11*, 37.

(15) Tran, T. T.; Elbadawi, C.; Totonjian, D.; Lobo, C. J.; Grosso, G.; Moon, H.; Englund, D. R.; Ford, M. J.; Aharonovich, I.; Toth, M. Robust multicolor single photon emission from point defects in hexagonal boron nitride. *ACS Nano* **2016**, *10*, 7331−7338.

(16) Exarhos, A. L.; Hopper, D. A.; Grote, R. R.; Alkauskas, A.; Bassett, L. C. Optical Signatures of Quantum Emitters in Suspended Hexagonal Boron Nitride. *ACS Nano* **2017**, *11*, 3328−3336.

(17) Chejanovsky, N.; Rezai, M.; Paolucci, F.; Kim, Y.; Rendler, T.; Rouabeh, W.; Fávaro de Oliveira, F.; Herlinger, P.; Denisenko, A.; Yang, S.; et al. Structural Attributes and Photodynamics of Visible Spectrum Quantum Emitters in Hexagonal Boron Nitride. *Nano Lett.* **2016**, *16*, 7037−7045.

(18) Jungwirth, N. R.; Calderon, B.; Ji, Y.; Spencer, M. G.; Flatté, M. E.; Fuchs, G. D. Temperature Dependence of Wavelength Selectable Zero-Phonon Emission from Single Defects in Hexagonal Boron Nitride. *Nano Lett.* **2016**, *16*, 6052−6057.

(19) Martínez, L.; Pelini, T.; Waselowski, V.; Maze, J.; Gil, B.; Cassabois, G.; Jacques, V. Efficient single photon emission from a high-purity hexagonal boron nitride crystal. *Phys. Rev. B: Condens. Matter Mater. Phys.* **2016**, *94*, 121405.

(20) Toth, M.; Aharonovich, I. Single photon sources in atomically thin materials. *Annu. Rev. Phys. Chem.* **2019**, *70*, 123−142.

(21) Grosso, G.; Moon, H.; Lienhard, B.; Ali, S.; Efetov, D. K.; Furchi, M. M.; Jarillo-Herrero, P.; Ford, M. J.; Aharonovich, I.; Englund, D. Tunable and high-purity room temperature single-photon emission from atomic defects in hexagonal boron nitride. *Nat. Commun.* **2017**, *8*, 705.

(22) Noh, G.; Choi, D.; Kim, J.-H.; Im, D.-G.; Kim, Y.-H.; Seo, H.; Lee, J. Stark Tuning of Single-Photon Emitters in Hexagonal Boron Nitride. *Nano Lett.* **2018**, *18*, 4710−4715.

(23) Vogl, T.; Lecamwasam, R.; Buchler, B. C.; Lu, Y.; Lam, P. K. Compact Cavity-Enhanced Single-Photon Generation with Hexagonal Boron Nitride. *ACS Photonics* **2019**, *6*, 1955−1962.

(24) Li, X.; Scully, R. A.; Shayan, K.; Luo, Y.; Strauf, S. Near-Unity Light Collection Efficiency from Quantum Emitters in Boron Nitride by Coupling to Metallo-Dielectric Antennas. *ACS Nano* **2019**, *13*, 6992−6997.

(25) Exarhos, A. L.; Hopper, D. A.; Patel, R. N.; Doherty, M. W.; Bassett, L. C. Magnetic field-dependent quantum emission in hexagonal boron nitride at room temperature. *Nat. Commun.* **2019**, *10*, 222.

(26) Tawfik, S. A.; Ali, S.; Fronzi, M.; Kianinia, M.; Tran, T. T.; Stampfl, C.; Aharonovich, I.; Toth, M.; Ford, M. J. First-principles investigation of quantum emission from hBN defects. *Nanoscale* **2017**, *9*, 13575−13582.

(27) Sajid, A.; Reimers, J. R.; Ford, M. J. Defect states in hexagonal boron nitride: Assignments of observed properties and prediction of properties relevant to quantum computation. *Phys. Rev. B: Condens. Matter Mater. Phys.* **2018**, *97*, No. 064101.

(28) Abdi, M.; Chou, J.-P.; Gali, A.; Plenio, M. B. Color centers in hexagonal boron nitride monolayers: A group theory and ab initio analysis. *ACS Photonics* **2018**, *5*, 1967−1976.

(29) Xu, Z.-Q.; Elbadawi, C.; Tran, T. T.; Kianinia, M.; Li, X.; Liu, D.; Hoffman, T. B.; Nguyen, M.; Kim, S.; Edgar, J. H.; et al. Single photon emission from plasma treated 2D hexagonal boron nitride. *Nanoscale* **2018**, *10*, 7957−7965.

(30) Vogl, T.; Campbell, G.; Buchler, B. C.; Lu, Y.; Lam, P. K. Fabrication and deterministic transfer of high-quality quantum emitters in hexagonal boron nitride. *ACS Photonics* **2018**, *5*, 2305−2312.

(31) Choi, S.; Tran, T. T.; Elbadawi, C.; Lobo, C.; Wang, X.; Juodkazis, S.; Seniutinas, G.; Toth, M.; Aharonovich, I. Engineering

DOI: 10.1021/acsphotonics.9b01707
ACS Photonics 2020, 7, 288−295

and localization of quantum emitters in large hexagonal boron nitride layers. *ACS Appl. Mater. Interfaces* **2016**, *8*, 29642−29648.
(32) Ngoc My Duong, H.; Nguyen, M. A. P.; Kianinia, M.; Ohshima, T.; Abe, H.; Watanabe, K.; Taniguchi, T.; Edgar, J. H.; Aharonovich, I.; Toth, M. Effects of high-energy electron irradiation on quantum emitters in hexagonal boron nitride. *ACS Appl. Mater. Interfaces* **2018**, *10*, 24886−24891.
(33) Proscia, N. V.; Shotan, Z.; Jayakumar, H.; Reddy, P.; Cohen, C.; Dollar, M.; Alkauskas, A.; Doherty, M.; Meriles, C. A.; Menon, V. M. Near-deterministic activation of room-temperature quantum emitters in hexagonal boron nitride. *Optica* **2018**, *5*, 1128−1134.
(34) Ziegler, J.; Klaiss, R.; Blaikie, A.; Miller, D.; Horowitz, V. R.; Alemán, B. J. Deterministic Quantum Emitter Formation in Hexagonal Boron Nitride via Controlled Edge Creation. *Nano Lett.* **2019**, *19*, 2121−2127.
(35) Storn, R.; Price, K. Differential Evolution − A Simple and Efficient Heuristic for Global Optimization over Continuous Spaces. *Journal of Global Optimization* **1997**, *11*, 341−359.
(36) Vogl, T.; Doherty, M. W.; Buchler, B. C.; Lu, Y.; Lam, P. K. Atomic localization of quantum emitters in multilayer hexagonal boron nitride. *Nanoscale* **2019**, *11*, 14362−14371.
(37) Kotakoski, J.; Jin, C.; Lehtinen, O.; Suenaga, K.; Krasheninnikov, A. Electron knock-on damage in hexagonal boron nitride monolayers. *Phys. Rev. B: Condens. Matter Mater. Phys.* **2010**, *82*, 113404.
(38) Turiansky, M. E.; Alkauskas, A.; Bassett, L. C.; Van de Walle, C. G. Dangling bonds in hexagonal boron nitride as single-photon emitters. *Phys. Rev. Lett.* **2019**, *123*, 127401.
(39) Shotan, Z.; Jayakumar, H.; Considine, C. R.; Mackoit, M.; Fedder, H.; Wrachtrup, J.; Alkauskas, A.; Doherty, M. W.; Menon, V. M.; Meriles, C. A. Photoinduced modification of single-photon emitters in hexagonal boron nitride. *ACS Photonics* **2016**, *3*, 2490−2496.
(40) Nikolay, N.; Mendelson, N.; Özelci, E.; Sontheimer, B.; Böhm, F.; Kewes, G.; Toth, M.; Aharonovich, I.; Benson, O. Direct measurement of quantum efficiency of single-photon emitters in hexagonal boron nitride. *Optica* **2019**, *6*, 1084−1088.
(41) Mendelson, N.; Xu, Z.-Q.; Tran, T. T.; Kianinia, M.; Scott, J.; Bradac, C.; Aharonovich, I.; Toth, M. Engineering and Tuning of Quantum Emitters in Few-Layer Hexagonal Boron Nitride. *ACS Nano* **2019**, *13*, 3132−3140.
(42) Comtet, J.; Glushkov, E.; Navikas, V.; Feng, J.; Babenko, V.; Hofmann, S.; Watanabe, K.; Taniguchi, T.; Radenovic, A. Wide-Field Spectral Super-Resolution Mapping of Optically Active Defects in Hexagonal Boron Nitride. *Nano Lett.* **2019**, *19*, 2516−2523.
(43) Stern, H. L.; Wang, R.; Fan, Y.; Mizuta, R.; Stewart, J. C.; Needham, L.-M.; Roberts, T. D.; Wai, R.; Ginsberg, N. S.; Klenerman, D.; et al. Spectrally Resolved Photodynamics of Individual Emitters in Large-Area Monolayers of Hexagonal Boron Nitride. *ACS Nano* **2019**, *13*, 4538−4547.
(44) Chakravarthi, S.; Moore, C.; Opsvig, A.; Pederson, C.; Hunt, E.; Ivanov, A.; Christen, I.; Dunham, S.; Fu, K.-M. C. A window into NV center kinetics via repeated annealing and spatial tracking of thousands of individual NV centers. 2019, arXiv:1907.07793 [cond-mat.mtrl-sci]. arXiv.org e-Print archive. https://arxiv.org/abs/1907.07793 (accessed Dec 3, 2019).

DOI: 10.1021/acsphotonics.9b01707
ACS Photonics 2020, 7, 288−295